Biophysical Journal, Volume *113*

Supplemental Information

Direct Numerical Simulation of Cellular-Scale Blood Flow in 3D Microvascular Networks

Peter Balogh and Prosenjit Bagchi

Supporting Information

Direct numerical simulation of cellular-scale blood flow in 3D microvascular networks

PETER BALOGH and PROSENJIT BAGCHI

Video files

Movie M1: Simulation of red blood cells flowing in the microvascular network shown in fig 1A in main article.

Movie M2: Simulation of red blood cells flowing in the microvascular network shown in fig. 1B in main article.

Movie M3: Close-up showing cell lingering near three bifurcations. The one at the top bifurcation causes temporary flow stoppage in the daughter vessels.

Movie M4: Close-up showing cell lingering near two bifurcations. The one on the right causes temporary flow stoppage in the daughter vessels.

Additional images of microvascular networks simulated

Additional images and an additional network simulated are presented in figs. S1-S3.

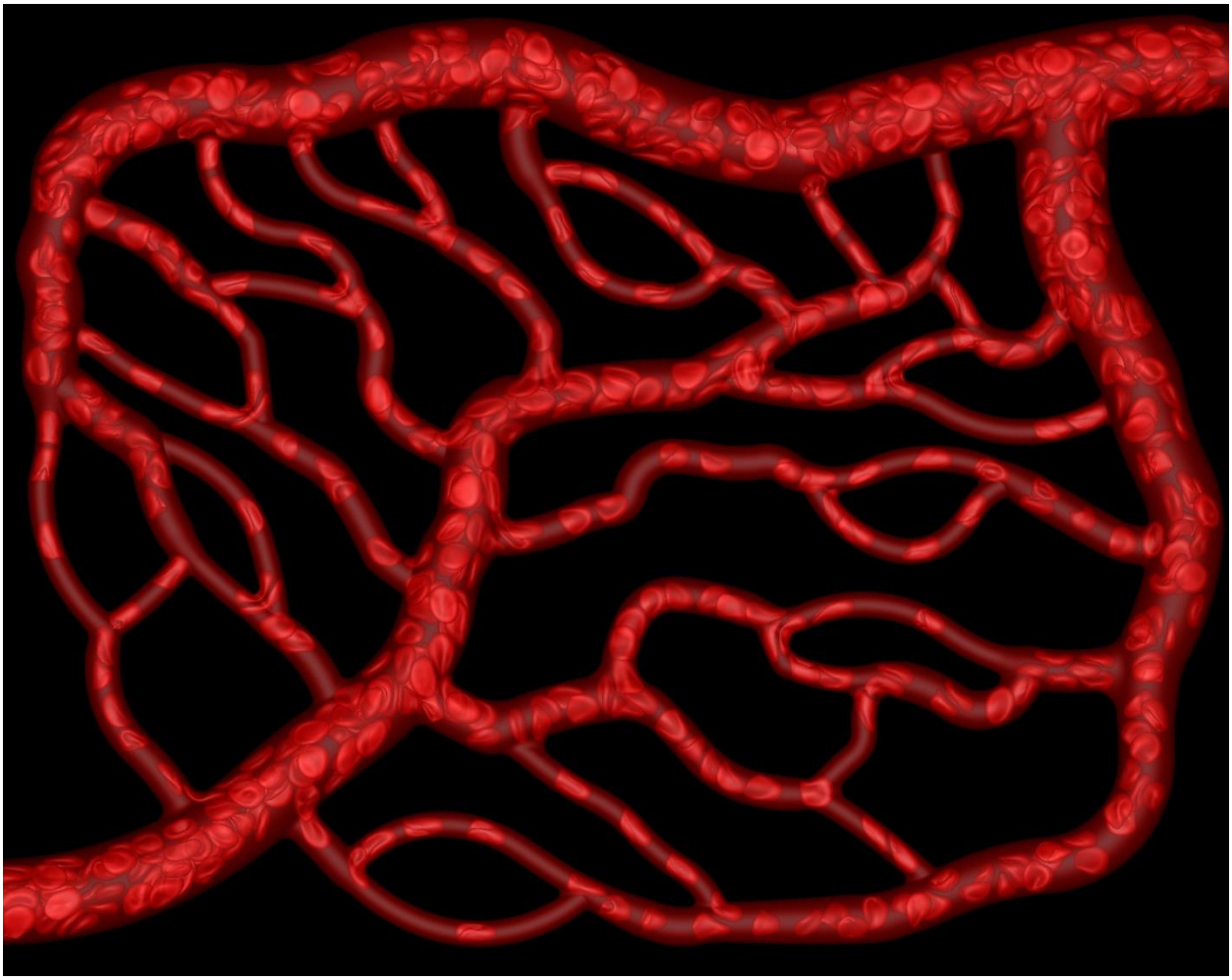

Figure S1: Additional snapshot of microvascular network shown in fig. 1A in main article.

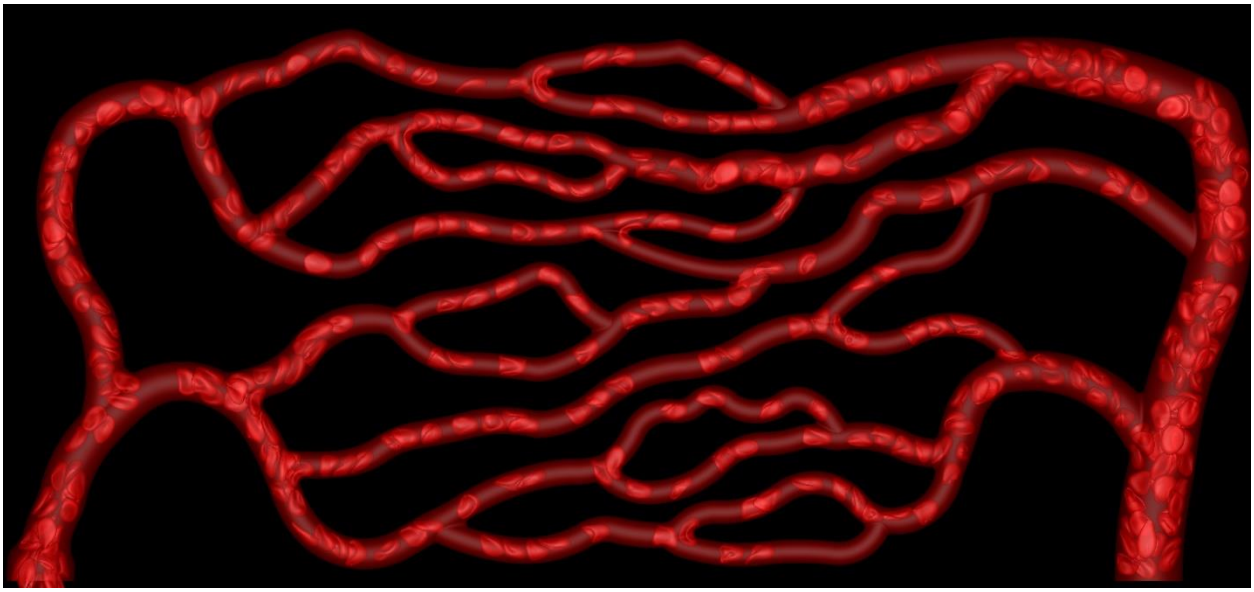

Figure S2: Additional snapshot of microvascular network shown in fig. 1B in main article.

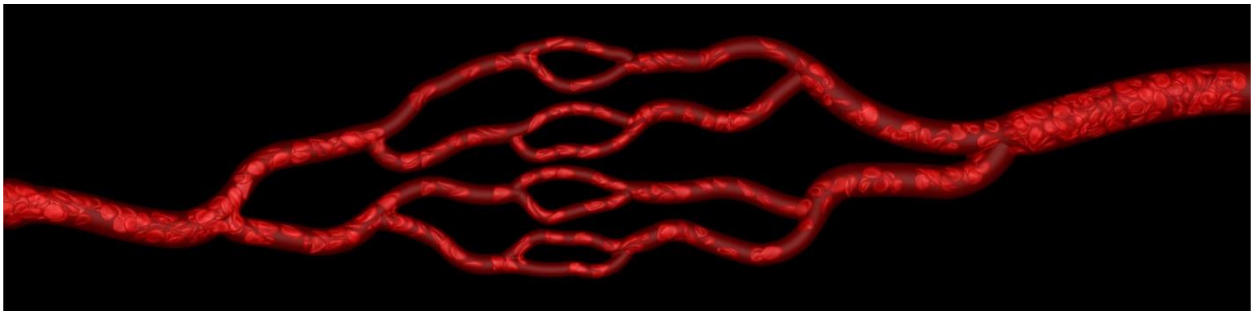

Figure S3: Additional (third) network simulated. Dimensions: 535 µm x 106 µm x 24 µm. Flow is from left to right.

Microvascular Network Design

In designing each of the three microvascular networks, Horton's Law was utilized to determine the relationships between vessel diameters at bifurcations and mergers. This law is defined as

$$\frac{D_n}{D_{n-1}} = 10^b \qquad \text{(S1)}$$

and a topology following this law is fractal in nature (1). The empirical constant *b* is taken as 0.1582, *D* is the vessel diameter, and the subscript *n* corresponds to the vessel order in the Strahler ordering system (1). For *b*=0.1582 the diameter ratio is approximately 1.43, however no distinction is made between the

arterial and venous sides of the network in Ref. (1). Since vessels of order *n* on the venous side are usually larger in diameter than their counterparts on the arterial side, we take this into account by using

$$\left.\frac{D_n}{D_{n-1}}\right|_{arterial} \approx 1.2 \qquad \left.\frac{D_n}{D_{n-1}}\right|_{venous} \approx 1.5 \tag{S2}$$

Within the Strahler ordering system the numbering begins at the capillaries, which are taken to be order 0. As the hierarchy proceeds upstream and downstream of these vessels, the order number increases to *n+1* when two vessels of the same order connect with each other. In many instances, connecting vessels are of the same order but have different diameters. In such cases an averaging is used in conjunction with the above diameter ratios to determine the appropriate vessel size. A similar approach is taken when connecting vessels are of a different order.

For the present work we did not investigate the effect of the 'b' exponent. The values of 'b' we used are average, not extreme values within the physiological range. As such, our networks are representative of 'average' physiological microvascular networks.

Our results are related in a more general way to the topology of the network, rather than being related to the geometry of a very specific type of network. That is, these results are not intended to be representative of what would be found, for example, only in a capillary network in the kidney of a rat. Rather, our conclusions and observations represent commonalities associated with general microvascular network topology, and offer insight in a more general way into the hemodynamic mechanisms present in cellular-scale network blood flow.

Different values of 'b' would result in networks with different diameter ratios between the mother and daughter branches of bifurcations. However, we do not feel that any of our conclusions or general observations would be different, barring drastic changes to this 'b' exponent representative of that beyond the physiological range, or of geometric anomalies in microvascular architecture. In light of this, an investigation into the effects of 'b' could be of interest. However, a significant computational undertaking would be required to properly study this issue, which is beyond the scope of this manuscript.

Numerical Methodology

The salient features of the numerical methodology relative to the present simulations are provided below. Additional details and validations can be found in (2). A schematic depicting various components associated with the numerical methodology is provided in Figure S4.

The underlying governing equations are the unsteady Stokes equations for a variable viscosity, constant density fluid, along with the conservation of mass:

$$\rho \frac{\partial \mathbf{u}}{\partial t} = -\nabla p + \nabla \cdot \mu[\nabla \mathbf{u} + \nabla \mathbf{u}^{\mathrm{T}}] + \boldsymbol{F} \quad \text{(S3)}$$

$$\nabla \cdot \mathbf{u} = 0 \quad \text{(S4)}$$

All interfaces are immersed into one computational domain that is discretized using a fixed, uniform, Cartesian Eulerian mesh. The governing equations are solved on this mesh using a projection method for the time integration and a staggered arrangement of variables in space. The presence of the complex vascular walls is simulated directly on this mesh by enforcing specific constraints on the Eulerian variables. The deformable interfaces are simulated on a separate Lagrangian mesh fixed to each cell (fig. S4-B), with information transferred to and from the main Eulerian grid using the front-tracking method.

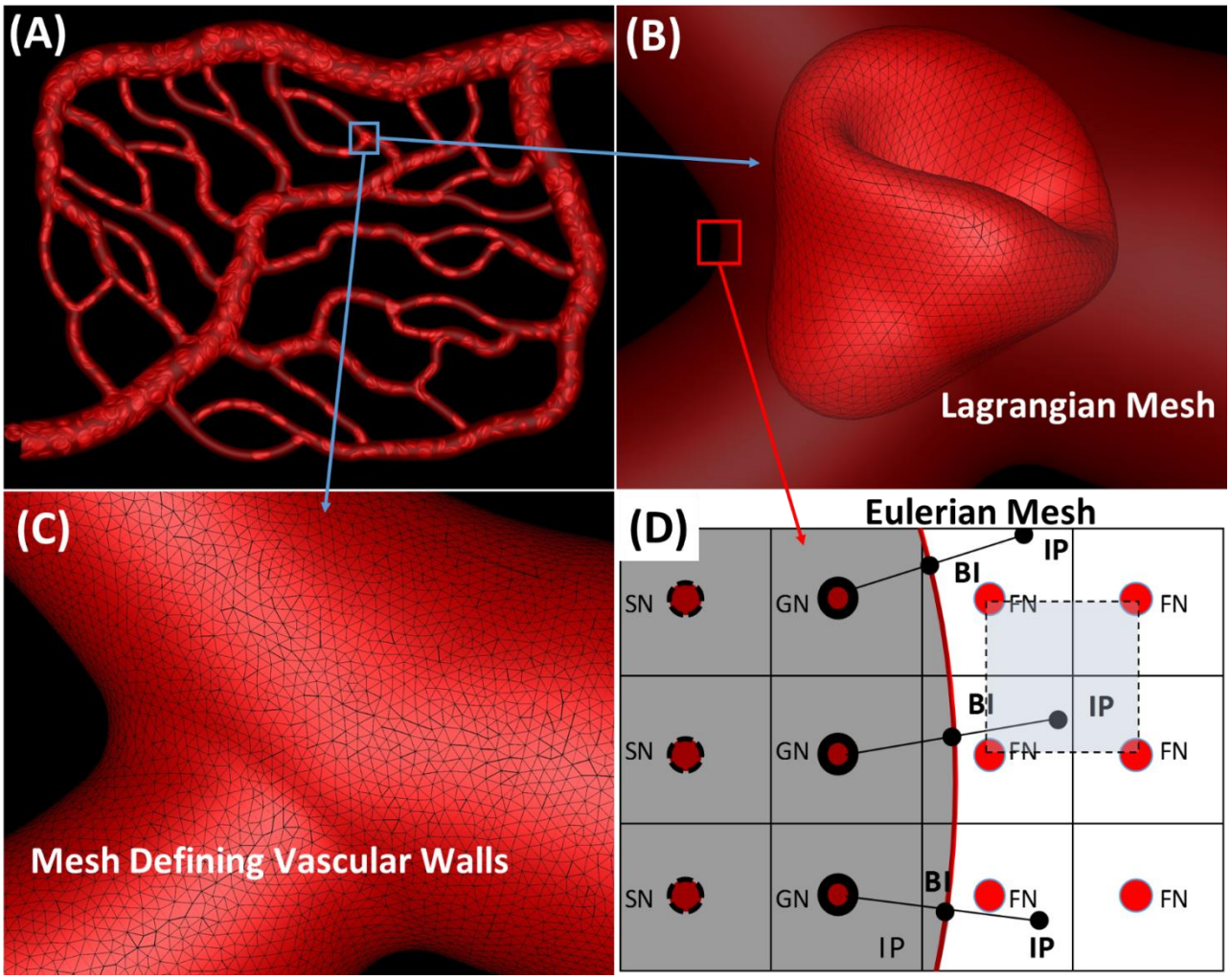

Figure S4: Schematic depicting various simulation components

(a.) Microvascular network simulation
(b.) Lagrangian mesh on which finite element computations are performed for RBC deformation
(c.) Mesh generated on surface of vascular network defining vessels walls when solving the governing fluid flow equations
(d.) Eulerian mesh on which the governing equations are solved. Eulerian mesh nodes are identified as Solid Nodes (SN), Ghost Nodes (GN), and Fluid Nodes (GN). Additional points utilized with the ghost node method are identified as Boundary Intercept (BI) and Image Points (IP).

For the deformable interfaces, the membrane of each RBC is discretized using Delaunay triangles (Figure S4-B), and the finite element method (FEM) is used to compute the stresses generated in the membrane resulting from shear deformation and area dilatation. In addition to this, the cell membrane also exerts a resistance against bending. Thus, the net membrane force ($\mathbf{f}_m$) is given by:

$$\mathbf{f}_m = \mathbf{f}_e + \mathbf{f}_b \quad \text{(S5)}$$

where $\mathbf{f}_e$ is the elastic tension at each vertex computed from the FEM and $\mathbf{f}_b$ is the bending force density. The means by which $\mathbf{f}_e$ and $\mathbf{f}_b$ are determined are now described.

For the FEM, the elements defined by the Delaunay triangles comprise the Lagrangian mesh, and each vertex (or node) is shared by five or six triangles. The cell shape and location is updated by advecting these nodes. At each node we compute the elastic force, $\mathbf{f}_e$, resulting from the membrane resistance against shearing deformation and area dilatation using:

$$\mathbf{f}_\mathrm{e} = \sum_n \int_{S_n} \frac{\partial \mathbf{N}}{\partial \mathbf{X}} \cdot \mathbf{P} \mathrm{d}S \quad \text{(S6)}$$

where **N** is a vector of shape functions, $\mathbf{P} = \varepsilon_1 \varepsilon_2 \boldsymbol{\tau} \cdot \mathbf{F}^{-\mathrm{T}}$ is the first Piola-Kirchhoff stress tensor, **X** is the original configuration of the membrane, and S_n is the area of each of the *n* triangles surrounding the node. To determine the shape functions (N_i), the displacement field **v** is expressed as $\mathbf{v} = N_\mathrm{i}\mathbf{v}_\mathrm{i}$, where the index i = 0,1,2 denotes the vertices of each triangle. Thus a linear variation of the displacement field is assumed within each element, and the shape functions are determined from the vertex coordinates. To determine **P**, we need to determine the principle stretch ratios ε_1 and ε_2, the principle stresses τ_1 and τ_2 comprising the stress tensor $\boldsymbol{\tau}$ in each element, and the deformation gradient **F**. ${\varepsilon_1}^2$ and ${\varepsilon_2}^2$ are the eigenvalues of $\mathbf{F} \cdot \mathbf{F}^{\mathrm{T}}$, so we first determine **F**, defined as $\mathbf{F} = {\partial \mathbf{x}}/{\partial \mathbf{X}}$, from the vertex coordinates, where **x** is the current configuration of the membrane. Once we have ε_1 and ε_2 we can determine the principle elastic tensions (or stresses) in the cell membrane as:

$$\tau_1 = \frac{1}{\varepsilon_2}\frac{\partial W_s}{\partial \varepsilon_1}, \qquad \tau_2 = \frac{1}{\varepsilon_1}\frac{\partial W_s}{\partial \varepsilon_2} \quad \text{(S7)}$$

Where W_s is the strain energy function of the membrane material. In this work we use the constitutive relation for W_s based on the work of Skalak et. al (3)

$$W_s = \frac{G_s}{4}\left[(I_1^2 + 2I_1 - 2I_2) + CI_2^2\right] \quad \text{(S8)}$$

Here G_S ~ 2-5x10^{-6} N/m is the membrane shear elastic modulus, CG_S is the area dilation modulus, and $I_1 = \varepsilon_1^2 + \varepsilon_2^2 - 2$ and $I_2 = \varepsilon_1^2\varepsilon_2^2 - 1$ are the strain invariants of the Green strain tensor defined as $\mathbf{E} = \left(\mathbf{F}^{\mathrm{T}} \cdot \mathbf{F} - \mathbf{I}\right)$. For an RBC, the shearing deformation can be significant, but the surface area dilation

is almost negligible. The parameter C is used to control the amount of surface area dilation, and a large value results in a small area dilation. Using each of these relations, the elastic force $\mathbf{f}_e$ is then computed at each node from Eq. S6. Additional details on the FEM are given in our prior work (4).

For the membrane resistance against bending, this is modeled following Helfrich's formulation for a bending energy, expressed as:

$$W_b = \frac{E_b}{2}\int_S (2\kappa - c_0)^2 \mathrm{d}S \tag{S9}$$

where E_b ~ 2-7 x 10^{-19} J is the bending modulus, κ is the mean curvature, c_0 is the spontaneous curvature, and *S* is the entire surface area of a cell (5). To evaluate the force density from this integral we use the following form, which can be derived from Eq. S9:

$$\mathbf{f}_b = E_b\left[(2\kappa + c_0)\left(2\kappa^2 - 2\kappa_g - c_0\kappa\right) + 2\Delta_{LB}\kappa\right]\mathbf{n} \tag{S10}$$

where κ_g is the Gaussian curvature, Δ_{LB} is the Laplace-Beltrami operator, and **n** is the normal vector. To evaluate the mean and Gaussian curvature at each node, a quadric surface is fitted to the node and its nearest neighbors. $\Delta_{LB}\kappa$ is then approximated on a small surface patch d*S* using the Gauss theorem, as $\left({}^{1}/_{\mathrm{d}S}\right)\int_l \nabla_S\kappa \cdot \mathbf{n}_l \mathrm{d}l$ where l denotes the patch boundary, d*S* the surface gradient, and $\mathbf{n}_l$ the unit normal to the boundary l. The gradient d*S* on a surface triangle can be obtained either by a linear interpolation of the surface and κ, or using the loop subdivision method. Further details on numerical computation of the bending force density are given in Ref. (6).

The resulting membrane forces computed from Eq. S5 are then coupled to the governing equations using the front-tracking method via the body force term, **F**, in Eq. S3, defined as:

$$\mathbf{F} = \int_S \mathbf{f}_m \delta(\mathbf{x} - \mathbf{x}')d\mathbf{x}' \tag{S11}$$

where δ is the three-dimension Dirac-delta function used to spread this singular force over a finite span of the surrounding fluid, and **x** and **x'** are the locations in the flow domain and on the cell surface *S*, respectively. We numerically approximate the delta function with a cosine function spanning four grid points around the cell boundary:

$$\delta(\mathbf{x} - \mathbf{x}') = \frac{1}{64\Delta^3}\prod_{i=1}^{3}\left[1 + \cos\frac{\pi}{2\Delta}(x_i - x_i')\right] \tag{S12}$$

where Δ is the Eulerian grid size.

We now describe the means by which the viscosity contrast between the hemoglobin and the plasma is modeled. The underlying structure of the numerical approach permits multiple fluids to be modeled within one computational framework. Mathematically the distinction is made between the separate fluids by means of an indicator function, *I*(x,t), which is zero outside a cell and one inside. This function is used to evolve the viscosity field μ(x,t) as the deformable cells change shape and acquire new locations. μ(x,t) written in terms of this indicator function is:

$$\mu(\mathbf{x},t) = \mu_p + \left(\mu_c - \mu_p\right) I(\mathbf{x},t) \tag{S13}$$

where μ_p and μ_c are the viscosities of the plasma and cytoplasmic fluids, respectively. It can be shown that the indicator function follows a Poisson equation as:

$$\nabla^2 I = \nabla \cdot \mathbf{G} \tag{S14}$$

where **G**(**x**,t) is an Eulerian variable constructed from the cell surface normal **n** as:

$$G(\mathbf{x},t) = \int_S \delta(\mathbf{x} - \mathbf{x}')\mathbf{n}\, \mathrm{d}S \tag{S15}$$

Equation S15 is solved to obtain *I* at each time step and update μ(**x**,t).

For the complex vascular network walls, the network geometry is first constructed using a standard CAD software in conjunction with *in vivo* image data. A mesh is then generated on the surface (Figure S4-C), which is used to define the vascular boundaries in discrete space. Constraints are enforced at the Eulerian grid points immediately exterior to the interface defined by this mesh (i.e. points identified as “ghost nodes”) such that a no-slip condition is achieved at the interface. These are formulated as follows (see Figure S4-D). Once the boundaries of the interface have been defined, the Eulerian nodes inside and outside the fluid domain are identified and labeled as fluid nodes (FN) and solid nodes (SN), respectively. The SNs that have at least one neighboring fluid node are identified as ghost nodes (GN). After the GNs have been identified, the boundary-intercept (BI) point for each ghost node is determined by locating the nearest point on the vascular wall. Following this, the image-points (IP) are determined for each GN, which are defined as the mirror image of the respective GN in the fluid domain, across the BI.

The constraints are enforced explicitly at each GN, and are formulated such that a known boundary condition $\mathbf{u}_{BI}$ is achieved at the BI. The value at the BI is taken to be the average of values at the GN and the IP. In general, the IPs do not coincide with the Eulerian nodes. A standard trilinear interpolant is used to obtain the velocity at the IP from the surrounding Eulerian nodes, and thus the constraint enforced on the velocity becomes:

$$\mathbf{u}_{GN} = 2\mathbf{u}_{BI} - \sum_{m=1}^{8} \beta_m \mathbf{u}_m \quad \text{(S16)}$$

where β_m are the weighting coefficients for the interpolation. This interpolation scheme results in a second-order accurate velocity field (2).

ADDITIONAL DATA on RESULTS

Comparison of predicted RBC shapes with experimental images

A wide variety of RBC shapes is observed in the simulations as the cells traverse the networks and undergo significant deformation. A few representative examples are provided in fig. S5, along with images from the experimental work (7).

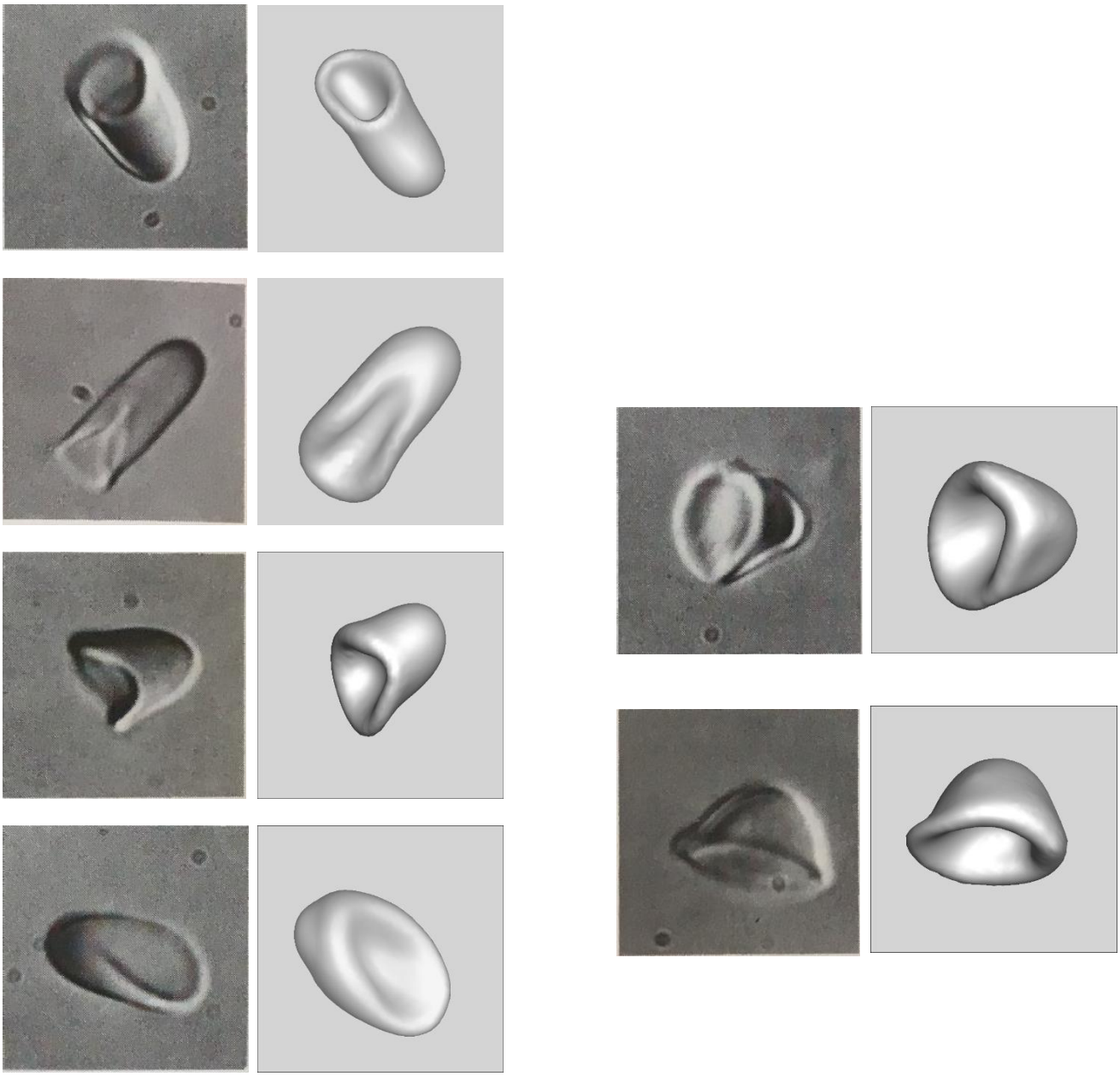

Figure S5: Comparison of various observed RBC shapes in the simulations with the experimental images of (7). For each comparison, the simulation image is on the right.

Additional comparisons with *In Vivo* data

The figures below provide additional quantitative comparisons between results obtained from our simulations and the *in vivo* data of (8). Specifically we compare the time averaged pressure drop per length ($\Delta P'$), wall shear stress (τ_w), and blood viscosity (μ) in Figure S6-A:C. The wall shear stress and viscosity are determined in an averaged sense, as in (8):

$$\tau_w = \frac{\Delta P' \cdot D}{4}$$

$$\mu = \frac{\Delta P' \cdot D^2}{\bar{V}}$$

where D is the vessel diameter and $\bar{V}$ is the bulk fluid velocity.

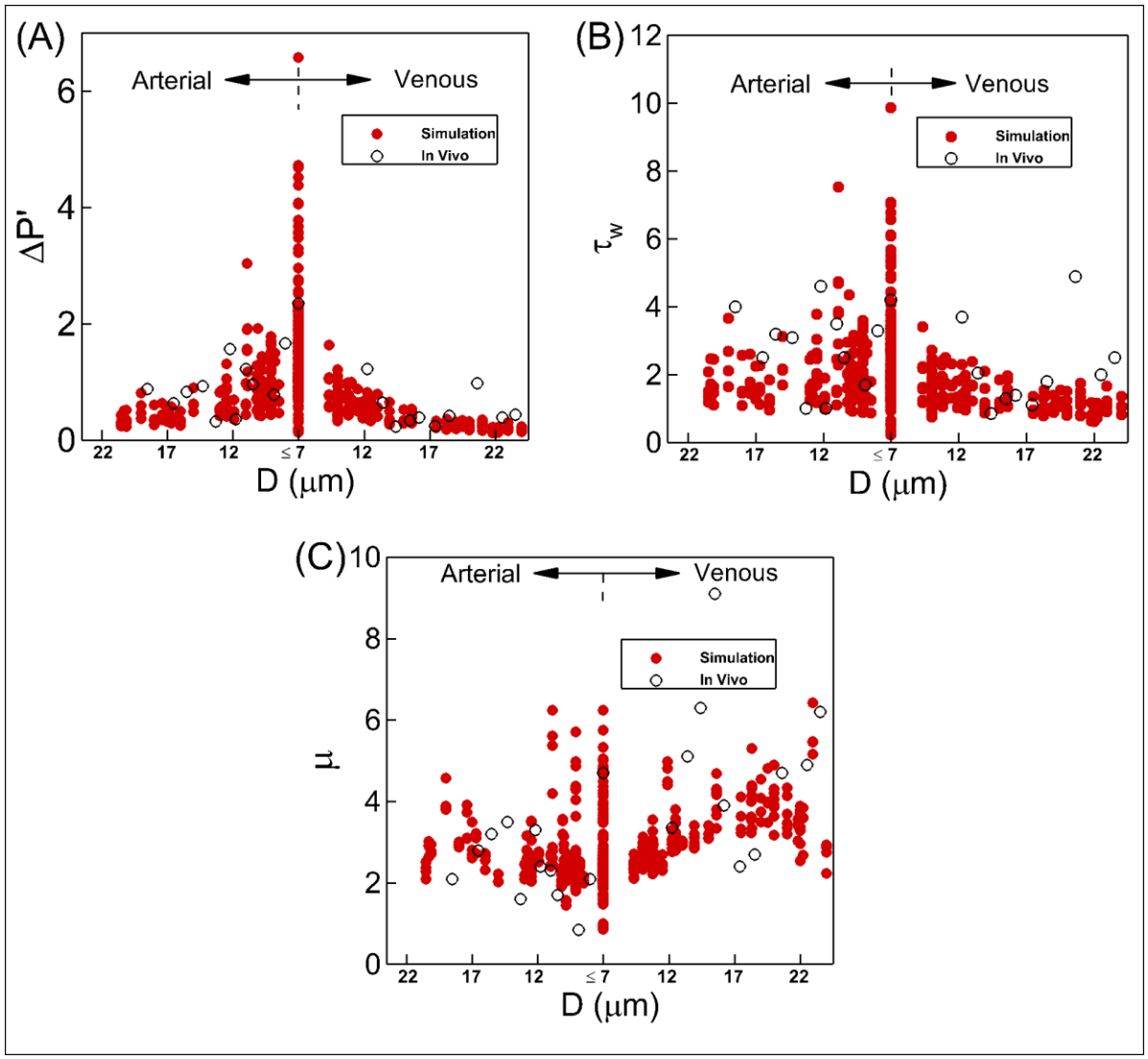

Figure S6 : Additional comparisons between simulation (red, filled circles) results and *in vivo* data (open black circles). (A) $\Delta P'$, Pa / μm; (B) τ_w, Pa ; (C) μ, cP

Spatial heterogeneity in flow rate

As a further demonstration of the spatial heterogeneity observed in our simulations, Figure S7 depicts the time-averaged flow rates as a function of vessel diameter.

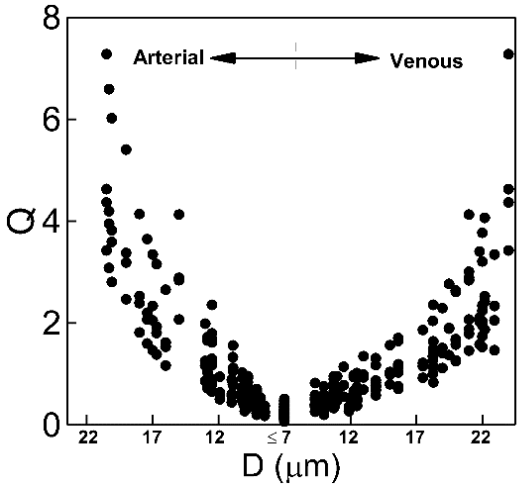

Figure S7: Arterio-venous distribution of time-averaged flow rates, Q, in m^3/sec x 10^{13}

Additional data on temporal heterogeneity

Examples of fluctuations in pressure drop per length and flow rate are provided in Figure S8 for a representative vessel. Similar to the hematocrit and resistance in the main article, to quantify the degree of temporal heterogeneity in theses quantities, the amplitude of fluctuation is determined for each. The distributions of these amplitudes are plotted in Figure S8-C:D scaled by the mean value for each individual vessel.

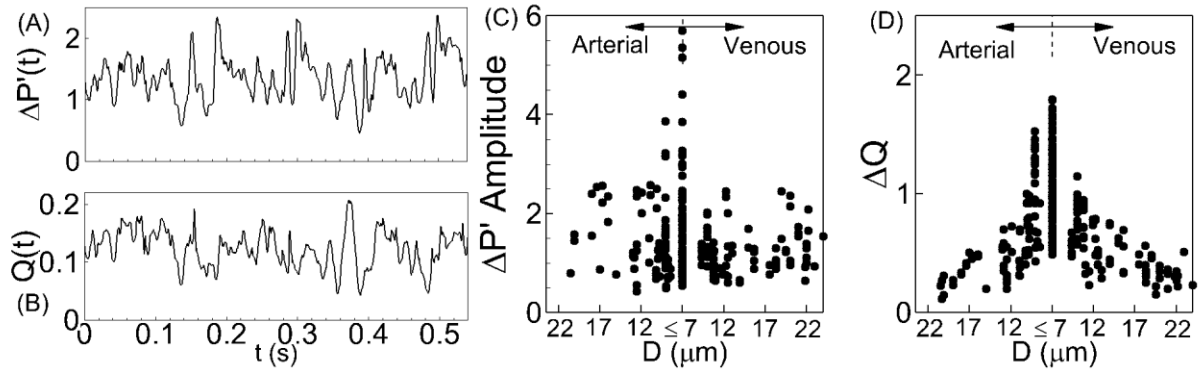

Figure S8. Temporal heterogeneity. A, B: Time history of pressure drop per length $\Delta P'(t)$ (in Pa/μm) and flow rate $Q(t)$ (in m^3/sec x 10^{13}) in one vessel in the network shown in fig. 1A in the main text. C, D: Amplitudes of temporal oscillations in $\Delta P'$ and Q in each vessel, scaled by the mean value for the respective vessel.

Additional data on RBC lingering

As mentioned in the main article, the RBC lingering phenomena is prominent. While it can be observed at all vascular bifurcations, the frequency is highest at the capillaries and decreases with decreasing vessel diameter. Additional images depicting lingering events at capillary bifurcations are provided in Figure S9, while lingering events occurring at bifurcations associated with larger vessels are provided in Figure S10.

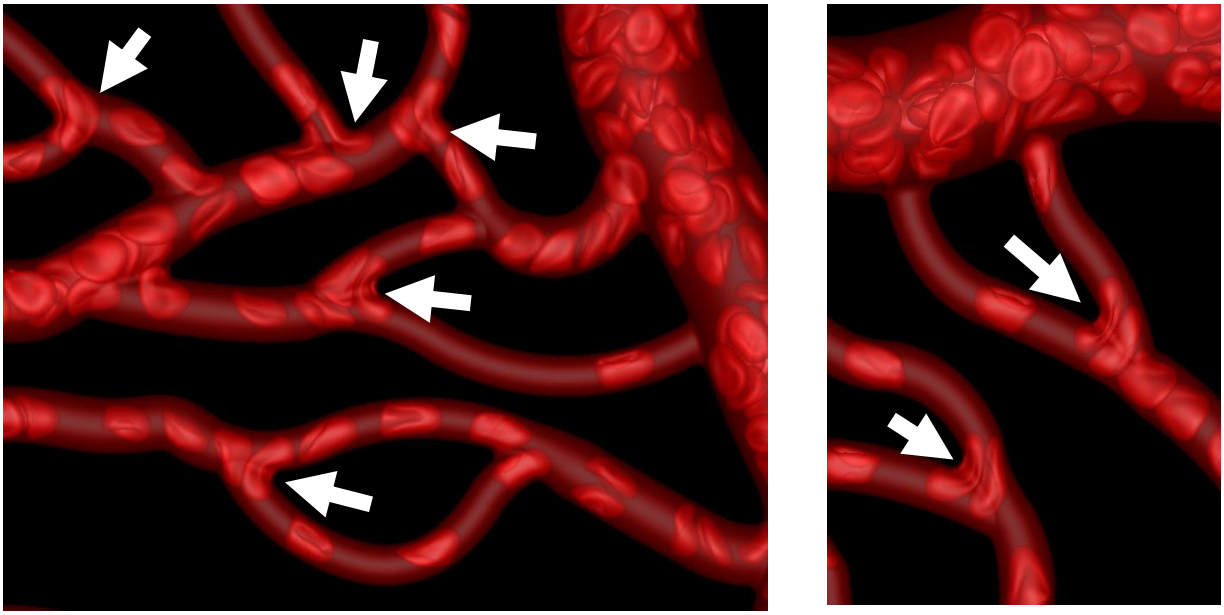

Figure S9: Additional examples of RBC lingering occurring at capillary bifurcations. Arrows are used to show the lingering.

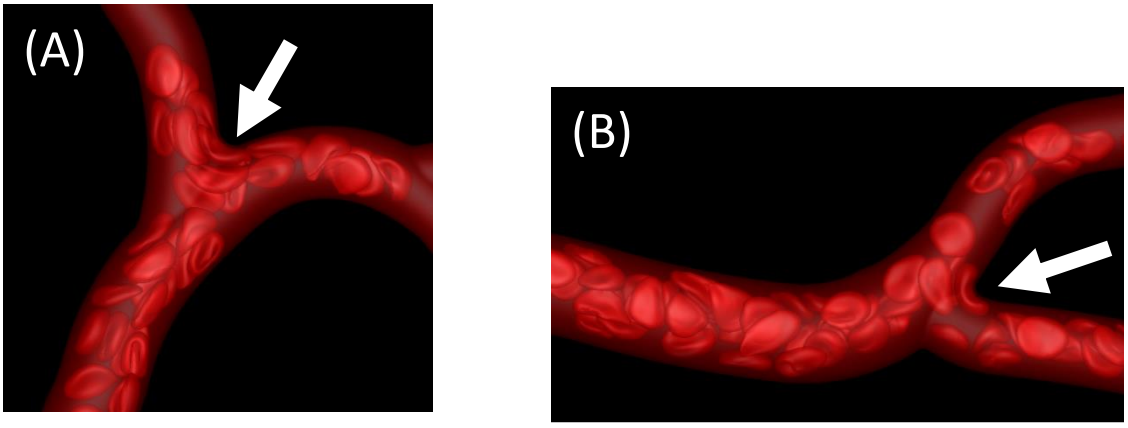

Figure S10: Examples of lingering events occurring at bifurcations associated with larger sized vessels. (A) mother vessel with 14µm diameter and daughter vessels with 11.5µm diameters; (B) mother vessel with 16µm diameter and daughter vessels with 12µm diameters.

Severe lingering events nearly stopping the flow in affected branches

During the most extreme events, lingering is observed to be so severe that it can nearly stop the flow in the affected branches. Examples of such events are provided in movies M3-M4.

Fig. S11 shows that upon such a severe lingering event (corresponding to video M3) the flow rates in the daughter vessels at about 0.23 s nearly become zero.

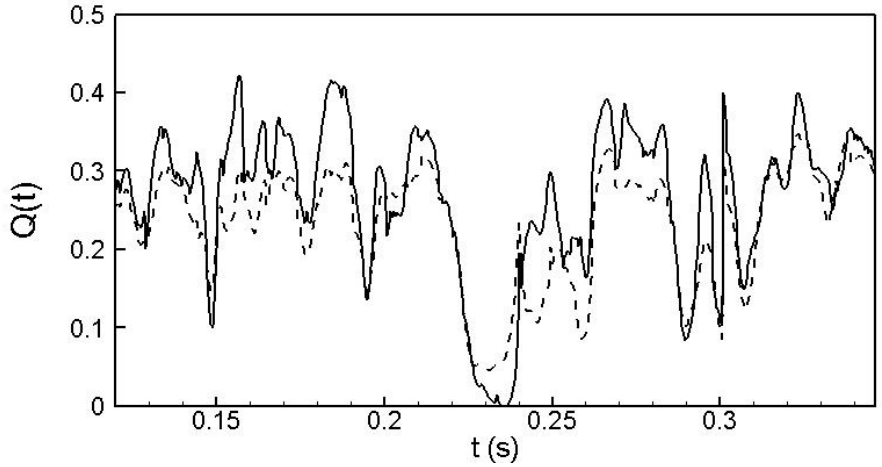

Fig. S11: Time series of flow rates in daughter branches upon a severe lingering at a bifurcation. Flow rates drop to nearly zero at about 0.23 s.

Additional examples of vessels with negative pressure-flow correlations

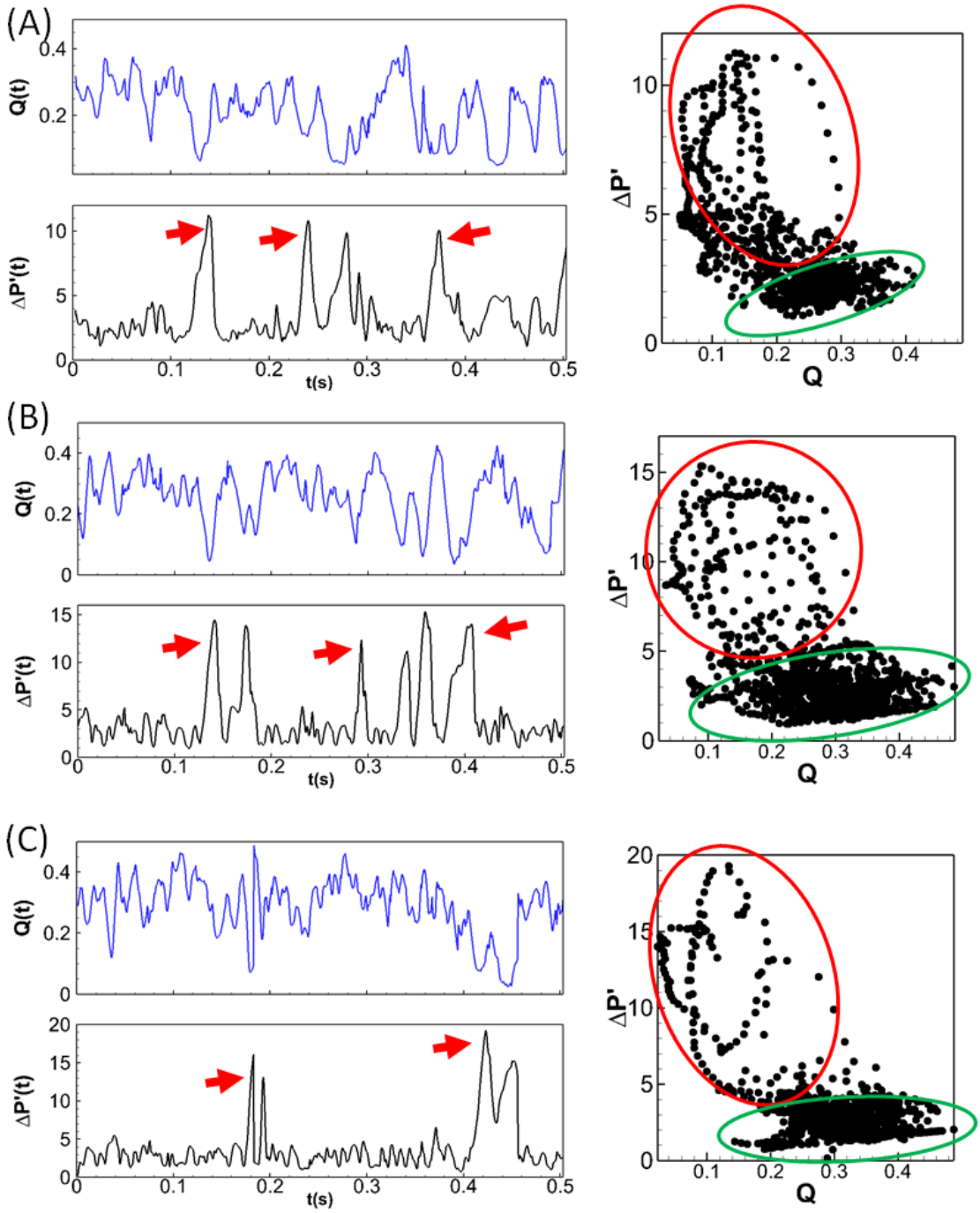

Figure S12. A-C: Additional examples of vessels with negative ΔP'-Q correlations. For each vessel, the time series of Q (m^3/s x 10^{13}) and $\Delta P'$ (Pa/μm) are plotted on the left. Red arrows indicate temporal increases in $\Delta P'$ corresponding to decreases in Q. On the right, for each vessel, data scatter of Q vs. $\Delta P'$ is provided. Red circles indicate data points corresponding to negative correlations, while the green circles indicate data points corresponding to positive correlations.

As discussed in the main text and shown in Figure 6A there, the lingering phenomena causes vessels to experience temporary sharp increases in ΔP' with corresponding decreases in Q. Examples from additional vessels illustrating this behavior are provided in Figure S12:A-C.

Additional examples of temporal "Spikes" in resistance

To further illustrate the consequence of the negative ΔP'-Q correlations where temporal "spikes" occur in the hydrodynamic resistance, examples from additional vessels showing these "spikes" are provided in Figure S13 A-C.

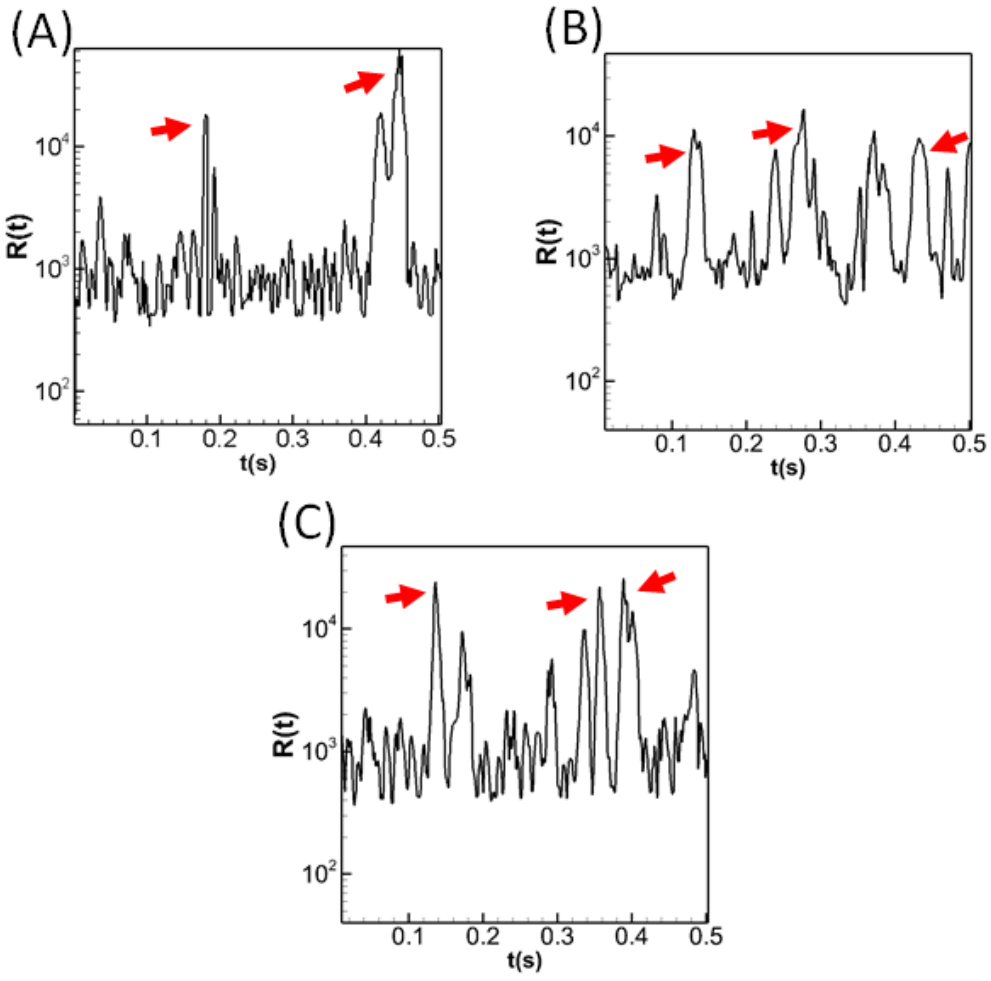

Figure S13. A-C: Additional examples of temporal spikes in hydrodynamic resistance as a consequence of the negative ΔP'-Q correlations. For each vessel, R (Pa/(m^3/s)/μm x 10^{-11}) is plotted vs. time. Red arrows draw attention to examples of "spikes" caused by lingering.

Additional examples of weak and negative resistance-hematocrit correlations

Figure S14. A-C below provides additional examples illustrating the relationship between R and H_t in different vessels.

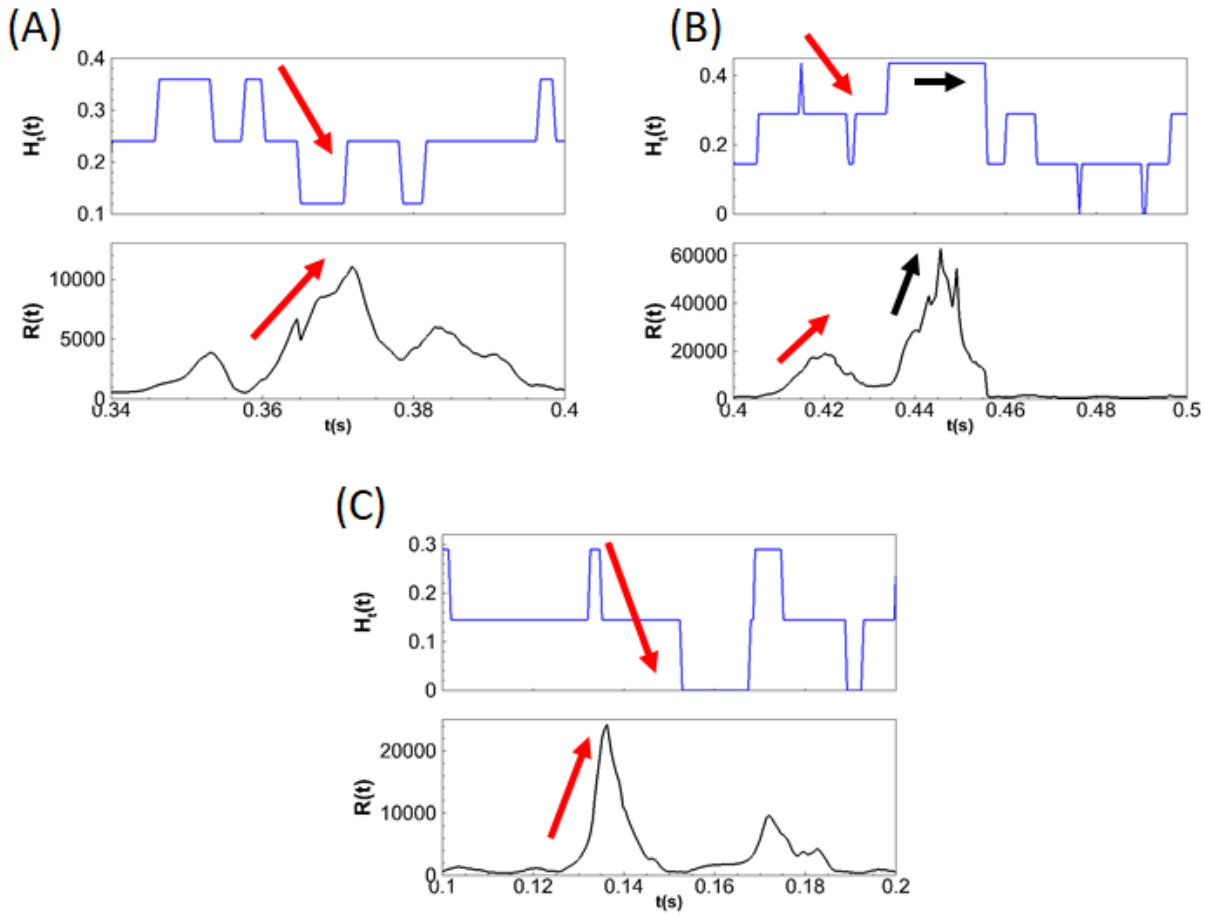

Figure S14. A-C: Time series of resistance (Pa/(m^3/s)/µm x 10^{-11}) and hematocrit in three different vessels to further illustrate the relationship between the two quantities. Red arrows denote times of negative correlations. Black arrows indicate times of weak positive correlations.

Additional information on increase in vessel hematocrit with a decrease in resistance

Here we further describe the process by which the hematocrit in a vessel on the venular side can increase but the resistance can decrease. As mentioned in the main article, a void is first formed in a capillary as a result of lingering. It then traverses the capillary and enters the outlet venule (Figure S15 B). In this outlet venule you thus have a volume flow rate contribution from capillary without a hematocrit contribution. In this downstream vessel this ultimately results in an increase in flow rate with little change in ΔP'. As this process repeatedly occurs, in the outlet venule there is a gradual decrease in resistance with a gradual increase in hematocrit (Figure S15 A).

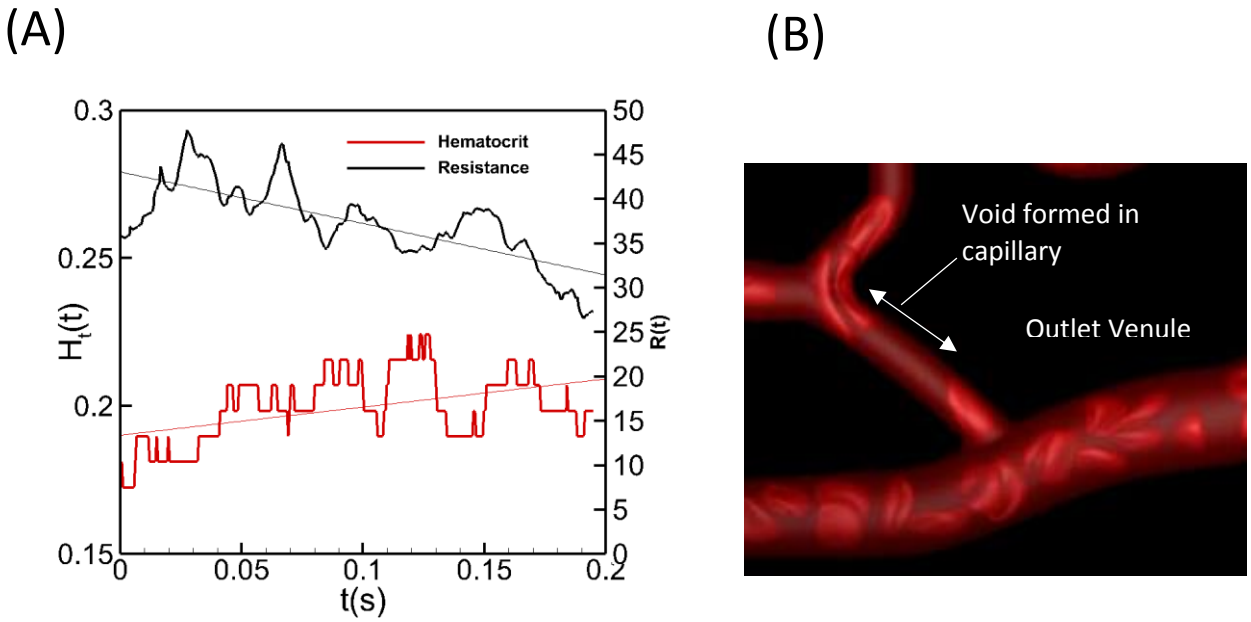

Figure S15: (A) Time-dependent hematocrit and resistance in outlet venule (shown in B) as an indirect result of void formation in the upstream capillary bifurcation. (B) Void formed in capillary, eventually traverses the vessel and discharges into the outlet venule.

References

1. Cassot F, Lauwers F, Fouard C, Prohaska S, Lauwers-Cances V (2006) A novel three-dimensional computer-assisted method for a quantitative study of microvascular networks of the human cerebral cortex. *Microcirculaton*, 13: 1-18.
2. Balogh P, Bagchi P (2017) A computational approach to modeling cellular-scale blood flow in complex geometry. *J. Comput. Phys*. 334: 280-307.
3. Skalak R, Tozeren A, Zarda RP, Chien S (1973) Strain energy function of red blood cell membranes. *Biophys. J.* 13: 245.
4. Yazdani A, Bagchi P (2013) Influence of membrane viscosity on capsule dynamics in shear flow. *J Fluid Mech* 718:569-595.
5. Zhong-Can OY, Helfrich W (1989) Bending energy of vesicle membranes: General expressions for the first, second, and third variation of the shape energy and applications to spheres and cylinders. *Phys. Rev.* A 3: 5280.
6. Yazdani AZ, Bagchi P (2012) Three-dimensional numerical simulation of vesicle dynamics using a front-tracking method. *Phys. Rev.* E 85: 056308.
7. Gaehtgens P, Duhrssen C, Albrecht K, (1980) Motion, deformation and interaction of blood cells and plasma during flow through narrow capillary tubes. *Blood Cells*, 6: 799-812.

8. Lipowsky HH, Kovalcheck S, Zweifach BW (1978) The distribution of blood rheological parameters in the microvasculature of cat mesentery. *Circulation Res*. 43(5): 738-749.